Pearce, C., Lewandowski, K., Kaczmarczyk, Ł., Athanasiadis, I. and Marshall, J. F. (2021) A computational framework for crack propagation in spatially heterogeneous materials. *Philosophical Transactions A: Mathematical, Physical and Engineering Sciences*, 379, 20200291. (doi: 10.1098/rsta.2020.0291).

This is the author's final accepted version.

There may be differences between this version and the published version. You are advised to consult the publisher's version if you wish to cite from it.

http://eprints.gla.ac.uk/227833/

Deposited on: 08 January 2021

Enlighten – Research publications by members of the University of Glasgow
http://eprints.gla.ac.uk

PHILOSOPHICAL TRANSACTIONS
OF THE ROYAL SOCIETY A
MATHEMATICAL, PHYSICAL AND ENGINEERING SCIENCES

A computational framework for crack propagation in spatially heterogeneous materials

Journal:	*Philosophical Transactions A*
Manuscript ID	RSTA-2020-0291.R1
Article Type:	Research
Date Submitted by the Author:	14-Dec-2020
Complete List of Authors:	Pearce, Chris; University of Glasgow Lewandowski, Karol; University of Glasgow Kaczmarczyk, Łukasz; University of Glasgow Athanasiadis, Ignatios; University of Glasgow Marshall, John Fraser; University of Glasgow
Issue Code (this should have already been entered and appear below the blue box, but please contact the Editorial Office if it is not present):	DM10202
Subject:	Mechanical engineering < ENGINEERING AND TECHNOLOGY, Biomedical engineering < ENGINEERING AND TECHNOLOGY
Keywords:	Finite element analysis, Functionally graded materials, Fracture, Configurational mechanics, Heterogeneous materials
Note: The following files were submitted by the author for peer review, but cannot be converted to PDF. You must view these files (e.g. movies) online.	
release_bone_energy_latex_source.zip	

SCHOLARONE™
Manuscripts

Author-supplied statements

Relevant information will appear here if provided.

Ethics

Does your article include research that required ethical approval or permits?:
This article does not present research with ethical considerations

Statement (if applicable):
CUST_IF_YES_ETHICS :No data available.

Data

It is a condition of publication that data, code and materials supporting your paper are made publicly available. Does your paper present new data?:
Yes

Statement (if applicable):
All additional code and data can be accessed via the following links:

https://bitbucket.org/likask/mofem-cephas
https://bitbucket.org/likask/mofem_um_fracture_mechanics

Conflict of interest

I/We declare we have no competing interests

Statement (if applicable):
CUST_STATE_CONFLICT :No data available.

Authors' contributions

This paper has multiple authors and our individual contributions were as below

Statement (if applicable):
Karol Lewandowski developed most of the contribution's C++ code and performed the computations.
Chris Pearce, Ignatios Athanasiadis and Lukasz Kaczmarczyk verified the analytical methods. John F Marshall provided CT scan data and insight regarding bones. All authors discussed the results and contributed to the final manuscript.

For Review Only

Noname manuscript No.
(will be inserted by the editor)

A computational framework for crack propagation in spatially heterogeneous materials

Karol Lewandowski · Łukasz Kaczmarczyk · Ignatios Athanasiadis · John F. Marshall · Chris J. Pearce

Received: date / Accepted: date

Abstract This paper presents a mathematical formulation and numerical modelling framework for brittle crack propagation in heterogeneous elastic solids. Such materials are present in both natural and engineered scenarios. The formulation is developed in the framework of configurational mechanics and solved numerically using the finite element method. We show that the methodology previously established for homogeneous materials without the need for any further assumptions. The proposed model is based on the assumption of maximal dissipation of energy and utilises the Griffith criterion; we show that this is sufficient to predict crack propagation in brittle heterogeneous materials, with spatially varying Young's modulus and fracture energy. Furthermore, we show that the crack path trajectory orientates itself such that it is always subject to Mode-I. The configurational forces and fracture energy release rate are both expressed exclusively in terms of nodal quantities, avoiding the need for post-processing and enabling a fully implicit formulation for modelling the evolving crack front and creation of new crack surfaces. The proposed formulation is verified and validated by comparing numerical results with both analytical solutions and experimental results. Both the predicted crack path and load-displacement response show very good agreement with experiments where the crack path was independent of material heterogeneity for those cases. Finally, the model is successfully used to consider the real and challenging scenario of fracture of an equine bone, with spatially varying material properties obtained from CT scanning.

Keywords Finite element analysis · functionally graded materials · fracture · configurational mechanics · heterogeneous materials

For Review Only

1 Introduction

The predictive modelling of crack propagation continues to generate significant scientific interest and represents an ongoing focus for computational mechanics research. The unstable and highly nonlinear nature of crack propagation in three-dimensional solids means that the development of a robust and objective modelling capability, that is able to capture the evolution of the crack front and creation of new crack surfaces, represents a considerable challenge.

This paper extends the authors' previous work for brittle fracture in solids that comprise homogeneous materials [34], to now consider spatially heterogeneous materials. Such materials are prevalent in both natural

Karol Lewandowski
Glasgow Computational Engineering Centre, The James Watt School of Engineering, University of Glasgow, Glasgow, G12 8QQ, UK
E-mail: karol.lewandowski@glasgow.ac.uk

John F. Marshall
Weipers Centre Equine Hospital, School of Veterinary Medicine, University of Glasgow, Glasgow, G61 1QH, UK

and engineered materials. Functionally Graded Materials (FGM) is a class of materials whose composition (and therefore material properties) vary spatially in a smooth fashion [35] and are used in many engineering applications [30, 50]. The advantage of FGMs is that they can be designed to achieve desired mechanical behaviour [14, 16]. Nevertheless, it is necessary to model their behaviour and failure characteristics when used in critical engineering applications. Numerical models have been proposed to investigate crack propensity and stress intensity factors in FGMs for various material distribution and multiple cracks, for instance [38, 2, 71, 61, 62]. Despite the breadth and importance of applications where these materials are present, numerical modelling of crack propagation is still in the early stages of development. The majority of well validated models available are limited to 2D analysis [39, 5, 52, 10]. For the 3D case, a phase field model has also been proposed [27]. However, such an approach is strongly mesh-size and step-size dependent, which could present an unsurmountable computational challenge for full scale applications.

Natural materials, such as bamboo, bone and skin exhibit spatially heterogeneous materials that also evolve over time. In particular, bone adapts to its mechanical environment (commonly referred to as bone remodelling); this is an on-going biological process of replacing old bone tissue with new bone, thus repairing fatigue damage [28]. This ability to repair bone micro-damage is essential for maintaining mechanical integrity. Therefore, variations in bone tissue quality and hence material properties can be observed at different locations and times of bone life. Consequently, there is a strong correlation between stress fractures and the adaptation process [28]. Furthermore, bone repair can be overwhelmed by load-induced bone densification that also increases brittleness and reduces fracture resistance [46].

This paper addresses the need for an energetically consistent model for crack propagation in heterogeneous materials. The formulation is developed in the framework of configurational mechanics and solved numerically using the finite element method. The concept of configurational forces was originally introduced by Eshelby [15]. Unlike physical forces, configurational forces act on the material manifold and represent the tendency of imperfections like cracks, voids or material inhomogeneities to move relative to the surrounding material. The past two decades have seen a growing interest in this approach for analysis of material imperfections [48] and in particular for evaluating the forces driving crack advancement [34, 63, 53]. However, until recently this approach has never been used to effectively assess configurational forces for cracking in heterogeneous bodies.

The model presented in this paper is based on the assumption of maximal dissipation of energy and utilises the Griffith criterion. We show that these assumptions are sufficient to predict crack propagation in brittle heterogeneous materials, using configurational mechanics. Additional configurational forces, arising from inhomogeneities [37] associated with spatially varying properties are introduced into the formulation. This allows for both the accurate assessment of the likelihood of a crack to propagate and to simulate the subsequent propagation of fractures. The model offers a computationally efficient 3D analysis tool for complex materials by means of a monolithic approach with relatively small number of finite elements.

Furthermore, the focus of this work is on the modelling of the physical process arising from a crack propagating through a solid with heterogeneous material and not on the particular choice of approximating the associated displacement discontinuity along the crack path. The framework proposed is not restricted to the particular implementation of the crack propagation algorithm (i.e. a mesh cutting algorithm in this paper). Other popular brittle crack propagation approaches such as XFEM and PUFEM, [6, 45, 3, 65] could adopt this framework by adding explicit approximation of material positions in order to incorporate the evaluation of configurational forces.

This article is structured as follows. After establishing the kinematic preliminaries in Section 2, Section 3 extends the authors' previous work for evolving crack propagation within the framework of configurational mechanics. Section 4 describes the finite element method implementation and briefly introduces a special element for capturing the singular stress field at the crack front. All the above components are brought together into a single framework and its performance is demonstrated using a series of numerical examples in Section 5, where the model is validated with experimental results for FGMs, as well as applying it to a full-scale model of equine bones using clinically available CT-scanning data.

For Review Only

2 Preliminaries

Figure 1 shows a section of a solid with an initial crack in the reference domain $\mathscr{B}_0$. As a result of loading, the crack extends and the body deforms elastically. Working within the framework of configurational mechanics [31, 37], it is convenient to decompose this behaviour into an extension of the crack in the material domain $\mathscr{B}_t$ followed by elastic deformation in the spatial domain Ω_t. The former is described by the mapping from the reference domain to the material domain $\boldsymbol{\Xi}$, whilst the latter is described by the mapping from the material to the spatial domain $\boldsymbol{\varphi}$ - Figure 1.

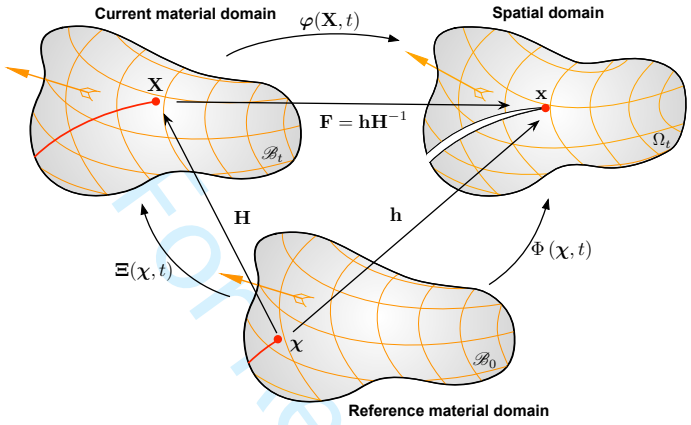

Fig. 1: Kinematics of crack propagation in elastically deforming body.

The material coordinates $\mathbf{X}$ are mapped onto the spatial coordinates $\mathbf{x}$ via the familiar deformation map $\boldsymbol{\varphi}(\mathbf{X},t)$. The physical displacement is:

$$\mathbf{u} = \mathbf{x} - \mathbf{X} \tag{1}$$

The reference material domain describes the body before crack extension. $\boldsymbol{\Xi}(\boldsymbol{\chi},t)$ maps the reference material coordinates $\boldsymbol{\chi}$ on to the current material coordinates $\mathbf{X}$, representing a configurational change, i.e. extension of the crack due to advancement of the crack front. $\boldsymbol{\Phi}$ maps the reference material coordinates $\boldsymbol{\chi}$ on to the spatial coordinates $\mathbf{x}$. The current material and spatial displacement fields are given as

$$\mathbf{W} = \mathbf{X} - \boldsymbol{\chi} \quad \text{and} \quad \mathbf{w} = \mathbf{x} - \boldsymbol{\chi} \tag{2}$$

$\mathbf{H}$ and $\mathbf{h}$ are the gradients of the material and spatial maps and $\mathbf{F}$ is the deformation gradient [31], defined as:

$$\mathbf{H} = \frac{\partial \boldsymbol{\Xi}}{\partial \boldsymbol{\chi}}, \quad \mathbf{h} = \frac{\partial \boldsymbol{\Phi}}{\partial \boldsymbol{\chi}}, \quad \mathbf{F} = \frac{\partial \boldsymbol{\varphi}}{\partial \mathbf{X}} = \mathbf{h}\mathbf{H}^{-1} \tag{3}$$

The time derivative of the physical displacement $\mathbf{u}$ and the deformation gradient $\mathbf{F}$ (material time derivative) are given as [31]:

$$\dot{\mathbf{u}} = \dot{\mathbf{w}} - \mathbf{F}\dot{\mathbf{W}} \qquad \dot{\mathbf{F}} = \nabla_{\mathbf{X}}\dot{\mathbf{x}} = \nabla_{\mathbf{X}}\dot{\mathbf{u}} = \nabla_{\mathbf{X}}\dot{\mathbf{w}} - \mathbf{F}\nabla_{\mathbf{X}}\dot{\mathbf{W}} \tag{4}$$

For Review Only

3 Fracture propagation

3.1 First and second laws of thermodynamics

The first law of thermodynamics can be expressed as

$$\int_{\partial\mathcal{B}_t} \dot{\mathbf{u}} \cdot \mathbf{t} \mathrm{d}S = \int_{\partial\Gamma} \gamma(\rho)\dot{A}_\Gamma + \frac{\mathrm{d}}{\mathrm{d}t}\int_{\mathcal{B}_t} \Psi(\mathbf{F},\rho)\mathrm{d}V \tag{5}$$

where the left hand side is the power of external work, the first term on the right hand side is the rate of crack surface energy and the last term is the rate of internal energy. $\mathbf{t}$ is the external traction vector, γ is the surface energy [Nm^{-1}], $\dot{A}_\Gamma$ is the change in the crack surface area, ρ is the density and Ψ is the volume specific free energy. The crack surface Γ comprises two crack faces and a crack front $\partial\Gamma$ - see Figure 2.

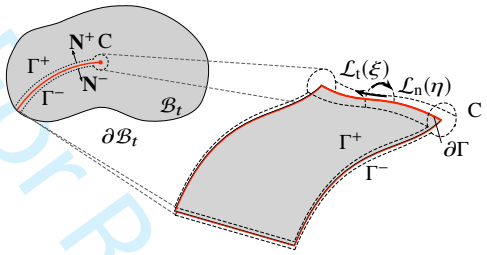

Fig. 2: Crack construction. In 2D (left) and in more detail in 3D (right).

The power of external work on the elastic body, with the use of Eq. (4), is given as:

$$\mathscr{P} = \int_{\partial\mathscr{B}_t} \dot{\mathbf{u}} \cdot \mathbf{t}\, \mathrm{d}\, S = \int_{\partial\mathscr{B}_t} \left\{\dot{\mathbf{w}} \cdot \mathbf{t} - \dot{\mathbf{W}} \cdot \mathbf{F}^{\mathrm{T}}\mathbf{t}\right\} dS \tag{6}$$

In [34], a kinematic relationship between the change in the crack surface area $\dot{A}_\Gamma$ and the crack front velocity $\dot{\mathbf{W}}$ was derived that is given as:

$$\dot{A}_\Gamma = \int_{\partial\Gamma} \mathbf{A}_{\partial\Gamma} \cdot \dot{\mathbf{W}} \mathrm{d}L \tag{7}$$

where $\mathbf{A}_{\partial\Gamma}$ is a dimensionless kinematic state variable that defines the orientation of the current crack front that can be considered a unit vector normal to the crack front and tangential to the crack surface. In deriving this expression, it was recognised that any change in the crack surface area $\dot{A}_\Gamma$ in the current material space can only occur due to motion of the crack front. Assuming that no dissipation of energy occurs within the volume of the body (i.e. restricted to the creation of new crack surfaces) and given that $\mathrm{d}\dot{V} = \nabla_{\mathbf{X}} \cdot \mathbf{W}\mathrm{d}V$, the change of the specific free energy can be expressed as:

$$\frac{\mathrm{d}}{\mathrm{d}t}\int_\Omega \Psi(\mathbf{F},\rho)\mathrm{d}\Omega = \int_\Omega \nabla_{\mathbf{X}}\dot{\mathbf{w}} : \mathbf{P} + \nabla_{\mathbf{X}}\dot{\mathbf{W}} : \Sigma + \mathbf{f}^{\mathrm{inh}} \cdot \dot{\mathbf{W}}\mathrm{d}\Omega \tag{8}$$

where

$$\mathbf{\Sigma} = \Psi(\mathbf{F},\rho)\mathbf{1} - \mathbf{F}^{\mathrm{T}}\mathbf{P}(\mathbf{F},\rho), \tag{9}$$

where $\mathbf{P}$ is the first Piola-Kirchhoff stress; in the case of heterogeneous materials, can be expressed as:

$$\mathbf{P} = \frac{\partial\Psi(\mathbf{F},\rho)}{\partial\mathbf{F}} = \left[\frac{\rho}{\rho_0^*}\right]^n \frac{\partial\Psi(\mathbf{F})}{\partial\mathbf{F}} \tag{10}$$

For Review Only

The parameter n is a characteristic exponent and ρ_0^* is the reference density. Although this form of the Piola-Kirchhoff stress was adopted from porous materials, such as bone [21], it can be used for generic heterogeneous materials. $\boldsymbol{\Sigma}$ is the Eshelby stress tensor and $\mathbf{f}^{\text{inh}}$ is an additional fictitious force that arises from variations in the density field and drives the crack front from dense to less dense material. $\mathbf{f}^{\text{inh}}$ is computed as follows:

$$\mathbf{f}^{\text{inh}} = \left(\frac{\partial \Psi}{\partial \mathbf{X}}\right)_{\text{expl.}} \tag{11}$$

where the explicit derivative of Ψ is defined by

$$\left(\frac{\partial \Psi}{\partial \mathbf{X}}\right)_{\text{expl.}} = \left.\frac{\partial \Psi}{\partial \rho}\right|_{(\mathbf{F}=\text{const})} \frac{\partial \rho}{\partial \mathbf{X}} \tag{12}$$

Making use of Equations (6), (7) and (8), Equation (5) can be reformulated as:

$$\begin{aligned}\int_{\partial \mathcal{B}_t} \left(\dot{\mathbf{w}} \cdot \mathbf{t} - \dot{\mathbf{W}} \cdot \mathbf{F}^{\mathrm{T}} \mathbf{t}\right) \mathrm{d}S = \int_{\partial \Gamma} \gamma \mathbf{A}_{\partial \Gamma} \cdot \dot{\mathbf{W}} \mathrm{d}L \\ + \int_{\mathcal{B}_t} \left(\mathbf{P} : \nabla_{\mathbf{X}} \dot{\mathbf{w}} + \boldsymbol{\Sigma} : \nabla_{\mathbf{X}} \dot{\mathbf{W}} + \mathbf{f}^{\text{inh}} \cdot \dot{\mathbf{W}}\right) \mathrm{d}V\end{aligned} \tag{13}$$

The spatial conservation law of linear momentum balance is repeated here:

$$\nabla_{\mathbf{X}} \cdot \mathbf{P} = 0 \; \forall \mathbf{X} \in \mathcal{B}_t, \quad \mathbf{P}\mathbf{N} = \mathbf{t} \; \forall \mathbf{X} \in \partial \mathcal{B}_t^{\sigma} \tag{14}$$

where $\partial \mathcal{B}_t^{\sigma}$ is the region of the boundary where tractions are applied and $\mathbf{N}$ is the outer normal to the surface. The equivalent material momentum balance is expressed as:

$$\nabla_{\mathbf{X}} \cdot \boldsymbol{\Sigma} = \mathbf{f}^{\text{inh}} \; \forall \mathbf{X} \in \mathcal{B}_t, \quad \boldsymbol{\Sigma}\mathbf{N} = \mathbf{F}^{\mathrm{T}} \mathbf{t} \; \forall \mathbf{X} \in \partial \mathcal{B}_t^{\sigma} \tag{15}$$

It is important to note that $\mathbf{f}^{\text{inh}} = \mathbf{0}$ in the case of homogeneous materials, with uniform density distribution. After applying the divergence theorem to Eq. (13) and recognising the momentum balance laws, we follow [34] to establish a local form of Eq. (13), which represents an expression for equilibrium of the crack front as

$$\dot{\mathbf{W}} \cdot (\gamma \mathbf{A}_{\partial \Gamma} - \mathbf{G}) = 0 \tag{16}$$

where the configurational force $\mathbf{G}$ is the driving force for crack propagation:

$$\mathbf{G} = \lim_{|\mathcal{L}| \to 0} \int_{\mathcal{L}_{\mathrm{n}}} \boldsymbol{\Sigma}\mathbf{N} \, \mathrm{d}L \tag{17}$$

From this equation, it is clear that the crack front is in equilibrium when the crack is not propagating, i.e. material velocity $\dot{\mathbf{W}}$ at the crack front is zero, or when the crack front is propagating and the configurational force is in equilibrium with the material resistance $\gamma \mathbf{A}_{\partial \Gamma}$.

It should be noted that crack front equilibrium is unaffected by material heterogeneities and does not depend on $\mathbf{f}^{\text{inh}}$. All terms in Eq. 16 are only evaluated at the crack front. However, it will be shown in Section 4.1 that, in a discrete setting, calculation of the nodal configurational forces involves a volume integral of the density gradient.

Since Eq. (16) has more than one solution at equilibrium, depending on whether the crack does or does not propagate, the formulation is supplemented by a straightforward criterion for crack growth, equivalent to Griffith's criterion [34]:

$$\phi(\mathbf{G}) = \mathbf{G} \cdot \mathbf{A}_{\partial \Gamma} - g_c/2 \leq 0 \tag{18}$$

where $g_c = 2\gamma(\rho)$ is a material parameter specifying the critical threshold of energy release per unit area of the crack surface Γ, also known as the Griffith energy. Note that in context of inhomogeneous materials it may depend on the density ρ. For a point on the crack front to satisfy the crack growth criterion, either $\phi < 0$ and $\dot{\mathbf{W}} = 0$, or $\phi = 0$, $\dot{\mathbf{W}} \neq 0$ and $\gamma \mathbf{A}_{\partial \Gamma} = \mathbf{G}$. The direction of fracture propagation is constrained by the second law

For Review Only

of thermodynamics. Here we assume that fracture takes place relatively fast, such that non-negative dissipation at the crack front can be expressed as

$$\mathcal{D} = \gamma \dot{\mathbf{W}} \cdot \mathbf{A}_{\partial\Gamma} = \dot{\mathbf{W}} \cdot \mathbf{G} \geq 0 \tag{19}$$

Finally, it is worth noting that the current framework is formulated within the realm of large displacements and large strains, hence it is generally valid under any assumption for strains and displacements.

3.2 Density field

The previous subsections have shown that fracture modelling of heterogeneous materials is influenced by the density distribution in the material configuration (see Eq. 10). This density field can be derived in a number of ways: in the case of FGMs, from a known function of spatial position; from image data of the material, such as computed tomography (CT) scans; in the case of a material that experiences remodelling, such as bone, from a separate numerical analysis [41, 32]. Previous examples in the literature of subject-specific modelling to assess the stresses and fracture resistance of heterogeneous bones can be found in [57, 25, 69]. Most algorithms that use CT voxel data have simply averaged [70] or integrated data onto finite elements, thereby supplying a constant density within each element volume [64, 60]. In this paper, the density data associated with each 3D voxel from CT scan data is spatially approximated.

In the numerical examples described later, the density in the reference configuration is prescribed as a function of spatial positions (FGM) and CT scan data for the bone example. It will be shown in the next section that, in order to evaluate the configurational forces at the crack front, it is necessary to have a spatially smooth density field. Therefore, discrete density data will need to be approximated as a smooth density field, and this will be achieved by adopting the Moving Weighted Least Squares (MWLS) method. This mapping approach was chosen since it offers higher regularity (i.e. higher derivatives exist) than when the field is directly approximated on the finite element mesh. Full details are given in [44].

4 Finite element modelling

In this work, three-dimensional domains are discretised with tetrahedral finite elements. Fields are approximated in the current material and current spatial spaces with hierarchical basis functions of arbitrary polynomial order, following the work of Ainsworth and Coyle [1].

$$\mathbf{X}^h(\boldsymbol{\chi}, t) = \boldsymbol{\Phi}(\boldsymbol{\chi})\tilde{\mathbf{X}}(t), \quad \mathbf{x}^h(\boldsymbol{\chi}, t) = \boldsymbol{\Phi}(\boldsymbol{\chi})\tilde{\mathbf{x}}(t) \tag{20}$$

$$\mathbf{W}^h(\boldsymbol{\chi}, t) = \boldsymbol{\Phi}(\boldsymbol{\chi})\dot{\tilde{\mathbf{W}}}(t), \quad \mathbf{w}^h(\boldsymbol{\chi}, t) = \boldsymbol{\Phi}(\boldsymbol{\chi})\dot{\tilde{\mathbf{w}}}(t) \tag{21}$$

where $\boldsymbol{\Phi}$ are shape functions, superscript h indicates approximation and $\tilde{(\cdot)}$ nodal values. Moreover, the smoothed density field is approximated by MWLS shape functions

$$\rho^{h,\mathrm{MWLS}}(\mathbf{X}, t) = \Phi^{\mathrm{MWLS}}(\mathbf{X})\tilde{\boldsymbol{\rho}}^h(\Xi(\boldsymbol{\chi}), t) \tag{22}$$

It should be noted that shape functions $\Phi^{\mathrm{MWLS}}(\mathbf{X})$ are evaluated at current material points, $\mathbf{X}$, rather than reference points, $\boldsymbol{\chi}$, as presented in Eq. (21) with the property of partition of unity. Since the density field is evaluated at $\mathbf{X}$, the approximation is independent of changes of the material configuration (i.e. changing mesh).

For Review Only

4.1 Fracture propagation

The residual force vector in the discretised spatial domain is expressed in the classical way as:

$$\begin{aligned} \mathbf{r}_{\mathrm{s}}^{\mathrm{h}}(\tilde{\boldsymbol{\rho}}(t), \tilde{\mathbf{x}}(t)) &= \tau \mathbf{f}_{\mathrm{ext,s}}^{\mathrm{h}} - \mathbf{f}_{\mathrm{int,s}}^{\mathrm{h}} \\ = \tau \int_{\partial \mathcal{B}_t^h} \boldsymbol{\Phi}^{\mathrm{T}} \mathbf{f}^{\mathrm{ext}} \mathrm{d}S - \int_{\mathcal{B}_t^h} \nabla_{\mathbf{X}} \boldsymbol{\Phi}^{\mathrm{T}} \mathbf{P}^{h,\mathrm{MWLS}} \mathrm{d}V &= \mathbf{0} \end{aligned} \tag{23}$$

where τ is the unknown scalar load factor, $\mathbf{f}_{\mathrm{ext,s}}^{\mathrm{h}}$ is the vector of externally applied forces and $\mathbf{f}_{\mathrm{int,s}}^{\mathrm{h}}$ is the vector of internal forces. The approximated Piola-Kirchhoff stress tensor for heterogeneous materials is expressed in terms of the density calculated using MWLS approximation, $\rho^{h,\mathrm{MWLS}}$, as follows:

$$\mathbf{P}^{\mathrm{h,MWLS}} = \mathbf{P}(\mathbf{F}^{\mathrm{h}}, \rho^{h,\mathrm{MWLS}}) \tag{24}$$

Discretisation of Eq. 16 establishes the material counterpart to Eq. 23, expressed as

$$\mathbf{r}_{\mathrm{m}}^{\mathrm{h}}(\tilde{\boldsymbol{\rho}}(t), \tilde{\mathbf{x}}(t)) = \mathbf{f}_{\mathrm{res}}^{\mathrm{h}} - \tilde{\mathbf{G}}^{\mathrm{h}} = \mathbf{0} \tag{25}$$

$\tilde{\mathbf{G}}^{\mathrm{h}}$ is the vector of nodal configurational forces that are only associated with nodes on the crack front:

$$\tilde{\mathbf{G}}^{\mathrm{h}} = \int_{\mathcal{B}_t^h} \nabla_{\mathbf{X}} \boldsymbol{\Phi}^{\mathrm{T}} \boldsymbol{\Sigma}^{h,\mathrm{MWLS}} \mathrm{d}V + \int_{\mathcal{B}_t^h} \boldsymbol{\Phi}^{\mathrm{T}} \frac{\partial \Psi^{h,\mathrm{MWLS}}}{\partial \rho^{h,\mathrm{MWLS}}} \left(\frac{\partial \rho^{h,\mathrm{MWLS}}}{\partial \mathbf{X}} \right) \mathrm{d}V \tag{26}$$

where the integration is restricted to elements adjacent to the crack front. These configurational forces are the driving force for crack propagation. It should be noted that the second term of $\tilde{\mathbf{G}}^{\mathrm{h}}$ reflects the influence of the spatially varying density. In the case of a homogeneous material, this second term would be zero. It should also be noted that this is only the case for the discretised configurational forces and that the continuum equivalent (Eq. 17) is unaffected by variation in the density field. $\mathbf{f}_{\mathrm{res}}^{\mathrm{h}}$ is the vector of nodal material resistance forces, given as:

$$\mathbf{f}_{\mathrm{res}}^{\mathrm{h}} = \frac{1}{2} \left(\tilde{\mathbf{A}}_{\Gamma}^{\mathrm{h}} \right)^{\mathrm{T}} \mathbf{g}_{\mathrm{c}}(\rho^{h,\mathrm{MWLS}}) \tag{27}$$

where $\mathbf{g}_{\mathrm{c}}$ is a vector of size equal to the number of nodes on the crack front. $\tilde{\mathbf{A}}_{\Gamma}^{\mathrm{h}}$ defines the current orientation of the crack front and is a matrix comprising direction vectors along the crack front that are normal to the crack front and tangent to the crack surface:

$$\tilde{\mathbf{A}}_{\Gamma}^{\mathrm{h}} = \int_{S_{\Gamma}^h} \boldsymbol{\Phi}^{\mathrm{T}} \frac{\partial A_{\Gamma}^h}{\partial \tilde{\mathbf{X}}} \mathrm{d}L \tag{28}$$

$\tilde{\mathbf{A}}_{\Gamma}^{\mathrm{h}}$ is evaluated by only integrating over S_{Γ}^{h} that defines the area of those triangular faces of tetrahedral elements that discretise the crack surface Γ^{h} adjacent to the crack front $\partial\Gamma^{\mathrm{h}}$. A_{Γ}^{h} is calculated as:

$$A_{\Gamma}^{\mathrm{h}} = \|\mathbf{N}(\tilde{\mathbf{X}})\| = \left\| \epsilon_{ijk} \frac{\partial \Phi^{\alpha}}{\partial \xi_0} \frac{\partial \Phi^{\beta}}{\partial \xi_1} \tilde{X}_j^{\alpha} \tilde{X}_k^{\beta} \right\| \tag{29}$$

where $\alpha, \beta \in \{0, 1, 2\}$ are the number of nodes of the triangle, $i, j, k \in \{0, 1, 2\}$ are material indices, $\boldsymbol{\epsilon}$ is the Levi-Civita tensor and ξ_0 & ξ_1 are the directions of the parent coordinate system of the triangular element. Moreover, the total number of degrees of freedom on element is $3(N_{\mathrm{base}} + 1)$ and the units of $\tilde{\mathbf{A}}_{\Gamma}^{\mathrm{h}}$ are $[\mathrm{m}^{-1}]$. $\mathbf{N}$ are the normals to the crack surface Γ.

The resulting discretised weak form of the two conservation equations (23 and 25) represent a set of coupled, nonlinear, algebraic equations that is solved in a monolithic manner using a Newton-Raphson scheme. In addition, an arc-length method is adopted to trace the dissipative load path for brittle fracture propagation, using a prescribed incremental change in crack area as a control.

For Review Only

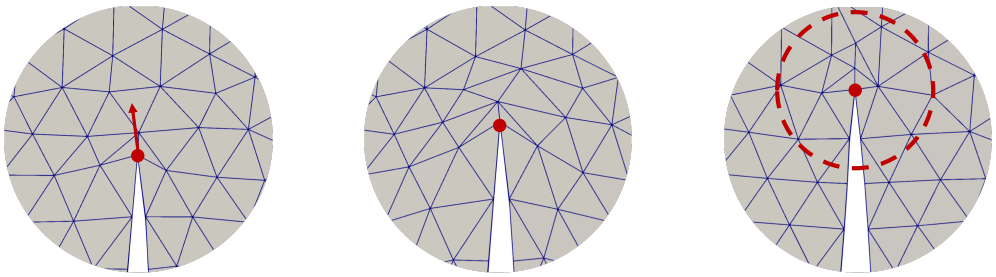

a) b) c)

Fig. 3: 2D representation of crack topology resolution prior to mesh cutting: a) Nodal configurational force at crack front. b) Crack front extension. c) Local modifications to the mesh, including cutting and remeshing.

4.2 Crack topology resolution

Continuous advancement of the crack front, and evolution of the crack surfaces, requires constant adjustments to, and adaptation of, the finite element mesh during an analysis. From a given crack configuration, the crack front is advanced by moving the nodes at the crack front in the direction of the configurational forces to establish crack front equilibrium, resulting in maximum energy dissipation (Eq. 19) - see Figure 3(a) and (b). This is achieved with only local changes to the mesh.

However, once the quality of the tetrahedral elements deteriorates, typically after 3-4 increments, the crack needs to be re-established by cutting the volume mesh by the new crack surfaces - Figure 3(c). This process involves only limited changes to the volume elements, since it is restricted to the elements immediately surrounding the crack. In addition, higher-order and p-adaptive elements based on a hierarchical approximation basis framework [33, 1] is adopted. Not only does this permit local enhancement of the approximation, it also mitigates the occasional existence of distorted elements in the mesh.

As part of this h - p - refinement scheme, the field of material parameters (density) is also mapped onto the new mesh. The data is stored on the vertices of a background mesh which does not change throughout the analysis. The data for any given material point of the new mesh is approximated using a meshless moving weighted least squares (MWLS) approach from the data stored on neighbouring vertices of the background mesh.

4.3 Singularity element

For the purposes of determining parameters such as stress intensity factors, it can be useful to reproduce the singular stress field at the crack front. However, conventional finite elements that adopt polynomial approximation functions are unable to do this. In this paper, a new type of finite element with hierarchical approximation functions that overcome this problem is utilised. This is inspired by the so-called quarter-point elements, originally developed in the 1970s, whereby the mid-node of all edges connected to the crack front node were shifted to the quarter-point [4, 26]. The result of this shift is a nonlinear mapping between natural (isoparametric) and local coordinates $\xi \rightarrow \mathbf{x}$ which produces the square root singularity. Stress and strain fields are dependent on the radial function of the crack front, approaching infinity at the front. A detailed derivation of the Jacobian for three-dimensional quarter-point elements can be found in, for example in [51]. The influence of using this element on calculating the stress at the crack front is investigated in Section 5.1.

5 Numerical examples

Several numerical examples are presented to illustrate each aspect of the proposed formulation. The accuracy of the calculated energy release rate and the performance of the singularity element formulation is demonstrated in Subsection 5.1 using a finite plate with a through-thickness crack and subjected to uniaxial stress. Moreover, in Section 5.2, the framework is compared against experimental and numerical data from literature for functionally graded materials. The final example considers fracture propagation of equine bone using experimental density data presented in Section 5.3.

5.1 Stress intensity calculations

To examine the calculation of configurational forces at the crack front in bodies with both homogeneous and heterogeneous density distributions, five numerical examples are presented. First, a simple quasi-two-dimensional plate with a through-thickness crack and homogeneous material distribution is considered. The convergence study utilises an approximate solution from the literature as a reference. Second, the proposed singularity elements are included for the same plate problem and their influence on the rate of convergence is presented. Third, the same problem is considered again but with a heterogeneous material distribution. The final two examples demonstrate the calculation of configurational forces for a more representative problem of an equine bone.

5.1.1 Finite plate with a horizontal crack

A finite plate with height, $h = 10$, thickness $t = 1$ and half width $b = 2.5$ and a horizontal through-thickness crack with half width $a = 1$, as presented in Figure 4(a), is considered. All input parameters are dimensionless. The plate is spatially discretised using 1384 tetrahedral elements and subjected to uniaxial stress in the longitudinal direction, as indicated in Figure 4(b). Displacements are constrained on three vertices to prevent rigid body motion.

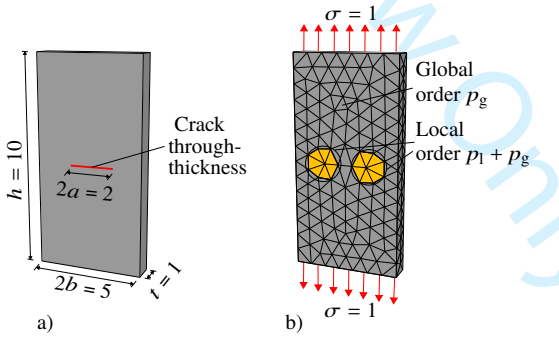

Fig. 4: Finite plate with a horizontal crack. a) Plate geometry with through thickness crack. b) Finite element mesh: grey elements have approximation order p_g; yellow elements have vertices at crack front and have approximation order $p_l + p_g$.

The purpose of this analysis is to calculate the Mode-I stress intensity factor K_I directly from the configurational forces and compare with the solution [58] for a finite plate:

$$K_I = \sigma\sqrt{\pi a}\left[\frac{1 - \frac{a}{2b} + 0.326(\frac{a}{b})^2}{\sqrt{1 - \frac{a}{b}}}\right] \tag{30}$$

For Review Only

where σ is the applied stress. Young's modulus E and Poisson's ratio ν are 1000 and 0.3, respectively.

Hierarchical approximation functions allow for global and local p - refinement without changing the mesh. In general, all tetrahedra of the mesh have a global order of approximation, p_g, with some elements subjected to local refinement of order p_l. All analyses presented were run using the same mesh with p - refinement varying from 1st-order to 6th-order so that $p_l + p_g \leq 7$. Assuming plane stress conditions, the Mode-I stress intensity factor, K_I, was calculated directly from the output configurational forces as:

$$K_I = \sqrt{GE} \tag{31}$$

where G is the change of elastic strain energy per unit area of crack growth. From Figure 5(a), it is evident that, for the same coarse mesh and number of nodes, the solution can improve drastically when the order of approximation is increased. The well known shear locking associated with first-order approximation is observed. The minimum error achieved is 0.50% for all the cases with total order of approximation $p_l + p_g = 7$. Therefore, it can be observed that using a low order of global approximation plus local p - refinement can achieve the same level of accuracy as using a global high order approximation, but with fewer degrees of freedom and lower computational cost.

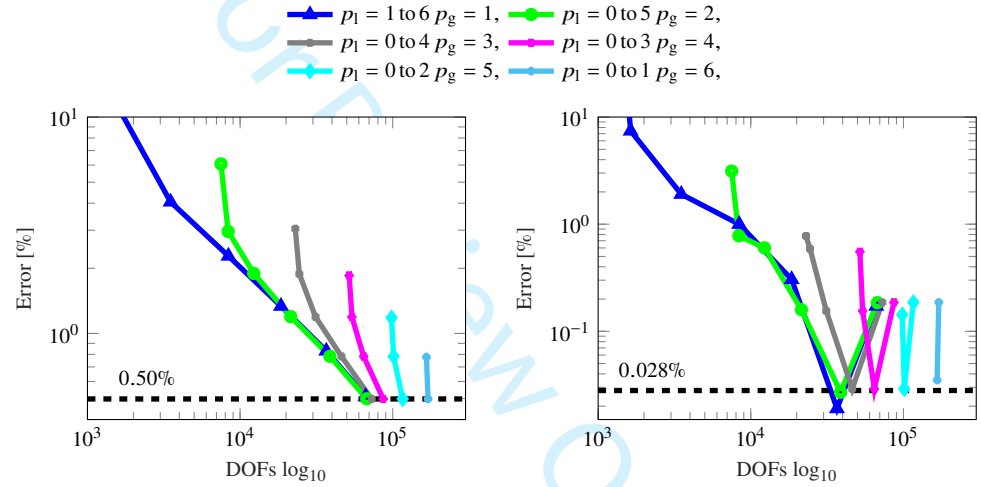

Fig. 5: Convergence plot for stress intensity factor K_I. Relative error (%) versus no. of DOF (log10) for a) using hierarchical approximation functions and b) using singularity elements.

From the results in Figure 5(b) it is evident that using singularity elements improves the convergence rate significantly and lowers the error by an order of magnitude, from 0.50% down to 0.028%. However, it can also be seen that for each combination of p - refinement, the error increases with further refinement after it reaches the minimum value. This suggests that the solution cannot be further improved by enhancing the order of approximation alone, since ultimately the model converges to a 3D solution. The difference between the stress calculated at the inner and outer nodes varies by up to 9%, whereas plane stress conditions assume the stress is constant throughout the thickness. Refining the element size and reducing the plate thickness will give better agreement with the assumptions used to obtain the analytical solution. Nevertheless, the results are considered sufficiently accurate for the purpose at hand.

Overall, these results indicate that singularity elements provide significant benefit, since they improve the accuracy of the solution with no extra cost. Furthermore, the difference in execution time for the analysis with and without their inclusion was negligible.

For Review Only

5.1.2 Heterogeneous material

So far the numerical examples have assumed homogenous material properties. Here we consider the effect of a heterogeneous density distribution (and therefore Young's modulus and fracture energy). Considering the same problem of the finite plate with horizontal crack, a density field $\rho(x, y, z) = 0.125y + 1$ is directly assigned to the integration (Gauss) points of each tetrahedral element. Exponent n and reference density ρ_0^* (see Eq. 10) are both equal to 1. As expected, configurational forces are induced at the crack front under load and, as explained in Section 4.1, these forces are influenced by the non-uniform density distribution. It is important to note that, in the case of heterogeneous materials, the stress intensity factors or J-integral are difficult to calculate or obtain experimentally [17]. Due to the inhomogeneities, the J-integral becomes path dependent and requires special correction terms to be computed [13, 11].

A straightforward verification can be performed by using a central difference numerical integration. The energy release rate for crack growth can be calculated as the change in elastic strain energy per unit area of crack growth [22]:

$$G = \frac{\partial \psi}{\partial a} \tag{32}$$

where ψ is the elastic energy of the system, and a is the crack length. This derivative can be approximated as:

$$\frac{\partial \psi}{\partial a} = \lim_{\Delta a \to 0} \frac{\psi(a + \Delta a) - \psi(a - \Delta a)}{2\Delta a} \tag{33}$$

where the elastic strain energies $\psi(a \pm \Delta a)$ is obtained from two additional analyses with horizontal cracks of lengths: $(a + \Delta a)$ and $(a - \Delta a)$, where Δa is a very small value. Next, knowing the resulting energy release rate with the crack length of a, a relative error can be calculated. It is worth noting that calculating the energy release rate using Eq. 33 is not suitable for any practical analyses, since it can be used only for simple crack paths, it is computationally expensive and potentially unstable for low values of Δa.

Twenty-four analyses, for different levels of p - refinement and values of Δa, have been undertaken in order to determine the error in the energy release rate. The results are presented in Figure 6, where it is apparent that the error in fracture energy release rate is converging to 0.3% with increasing levels of refinement. It is worth noting that a similar level of accuracy was attained for the homogeneous case. Achieving higher precision with this means of validation is difficult due to the accumulation of truncation, approximation and discretisation errors. Therefore, it can be concluded that the proposed estimation of fracture energy release rate for heterogeneous materials is obtained with a satisfactory level of accuracy.

5.2 Crack propagation in FGMs

The correct implementation and performance of the presented computational method is demonstrated by means of two 3D numerical examples of crack propagation in functionally graded materials. In order to validate the numerical results, we adopt examples reported by [40], who compared their analyses against experimental data [18, 59]. The examples consider crack propagation in graded beams under three-point bending. Figure 7 shows specimen geometries, discretisation and boundary conditions for two cases: (a) simple symmetric three-point bending and (b) considering offset loading which results in a mixed mode crack evolution. Discretisation is undertaken using 3D quadratic tetrahedral elements with an additional local p - refinement (increased polynomial degree) around the crack tip, where 3rd order polynomials are used. Throughout the analyses, the mesh adapts as the crack propagates according to h - p - refinement scheme as mentioned in Section 4.2.

The analyses consider two materials: homogeneous poly-methyl-methacrylate (PMMA) and linearly graded polymer, where Young's modulus E and fracture toughness K_{Ic} are linearly varying from top to bottom. The numerical values of material properties for PMMA are as follows: E = 2890 [MPa], ν = 0.4, K_{Ic} = 1.09 [MPa $\sqrt{\text{m}}$] and for the graded case values at top and bottom points are shown in Table 1. Note that due to current limitations of the implementation the Poisson's ratio is assumed to be constant (unlike in original work of [40] where the used ratio was varying from 0.39 to 0.41).

For Review Only

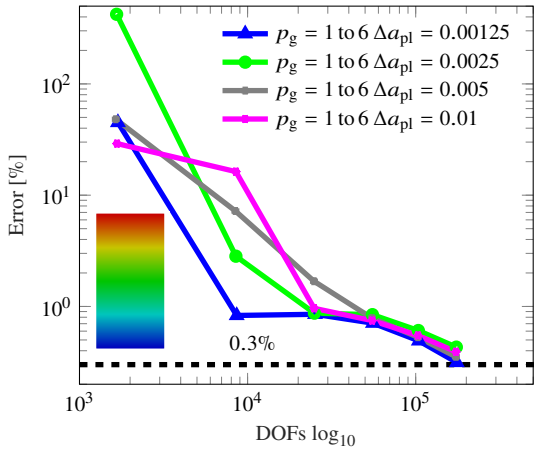

Fig. 6: Convergence plot for stress intensity factor K_I for heterogeneous density distribution. Relative error (%) versus no. of DOF (log10).

Y [mm]	E [MPa]	ν	K_{Ic} [MPa $\sqrt{m}$]
0	1780	0.4	0.99
60	4000	0.4	1.19

Table 1: Material parameters used for FGM simulations. Relationship between K_{Ic} and g_c can be found in Eq. 31.

The arc-length control is adopted to trace the nonlinear response, using an adaptive crack area increment with a target of $\Delta s = 5$ [mm^2] per load step. Figure 8 shows comparison of load versus crack mouth opening displacement (CMOD) curves for both a homogeneous and a functionally graded beam for Case 1 (symmetric loading) obtained by the presented approach and compared with results from the literature [40], with which there is good agreement. Due to symmetry, the crack is in pure Mode-I and therefore the resulting crack is a plane surface. It is evident that the material gradation results in an increased critical load P. Figure 9 presents a comparison of load versus CMOD curve for both a homogeneous and a functionally graded beam for Case 2 (mixed-mode). Once again, the numerical results from the presented work are compared to results from the literature [40]. It can be noticed that the peak loads and initial stiffness obtained by the proposed approach are slightly lower than those obtained in the literature. This can be explained by the influence of the initial crack. As shown in Figure 7 the initial crack is short and vertically aligned, in comparison to the resulting crack surfaces shown in 10, where the crack trajectory curves towards left hand side. In the first few loading steps the crack reorientates towards a pure Mode-I situation, therefore the initial load required for crack propagation is different than in the literature. A few load steps after the peak load, the curves are in very good agreement.

It can be noticed in both 3D views in Figures 9 and 10, that the density of the final FE mesh is increased along the crack surfaces due to mesh cutting and adaptive refinement triggered every three load steps. Nevertheless, the resulting meshes are relatively coarse for 3D analysis with 3515 and 8079 elements for Case 1 and Case 2, respectively.

Figure 10 shows comparison of the predicted crack path and experimental results for Case 2 (offset loading, leading to mixed mode loading at the crack front). The presented approach shows an excellent agreement with the experimentally obtained crack path and an improvement on previously documented 2D analyses [40]. Within the framework of linear elastic fracture mechanics, although spatially varying material properties has no effect on the crack path for these particular problems, the ultimate load is influenced.

For Review Only

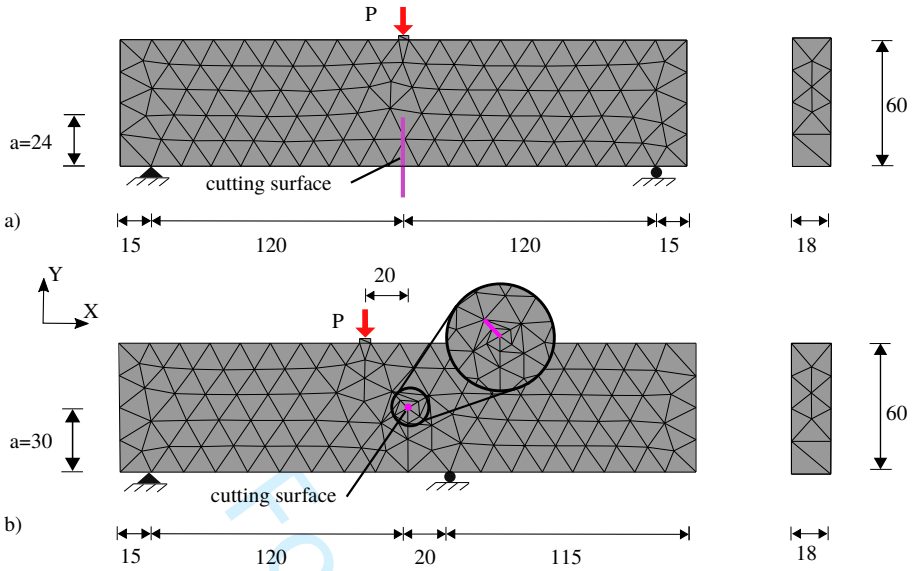

Fig. 7: FGM example: A crack in a beam subjected to three-point bending. Geometry, boundary conditions and initial discretisation for (a) Case 1: symmetric loading, (b) Case 2: offset loading. Units in [N], [mm]. Note that in both cases the total force P is applied in the form of uniformly distributed pressure on a block with dimensions: 2.25x4.5x18 [mm]. The initial meshes consists of 1751 and 1794 quadratic tetrahedral elements.

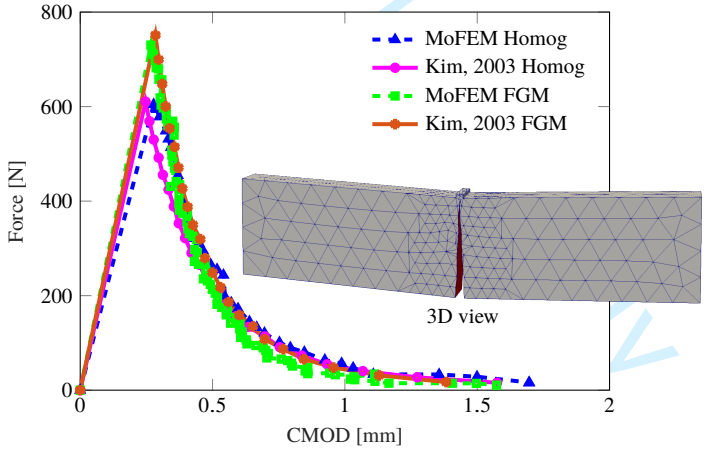

Fig. 8: Case 1: Comparison of Load - CMOD curves for homogeneous and FGM beams obtained by [40] and the present numerical analysis (MoFEM). 3D view of final crack surface and FE mesh.

5.3 Fracture energy release rate for metacarpal bone

The fracture of an equine 3rd metacarpal bone is now presented. Horse fatalities at racecourses are often directly or indirectly associated with a fracture, with the distal limb the most commonly affected site [54]. Most of these fractures occur due to the accumulation of tissue fatigue, as a result of repetitive loading [56],

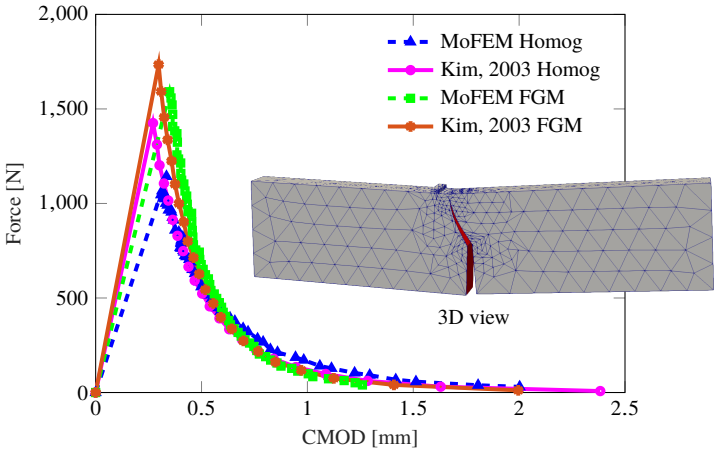

Fig. 9: Case 2: Comparison of Load - CMOD curves for homogeneous and FGM beams obtained by [40] and the present numerical analysis (MoFEM). 3D view of final crack surface and FE mesh.

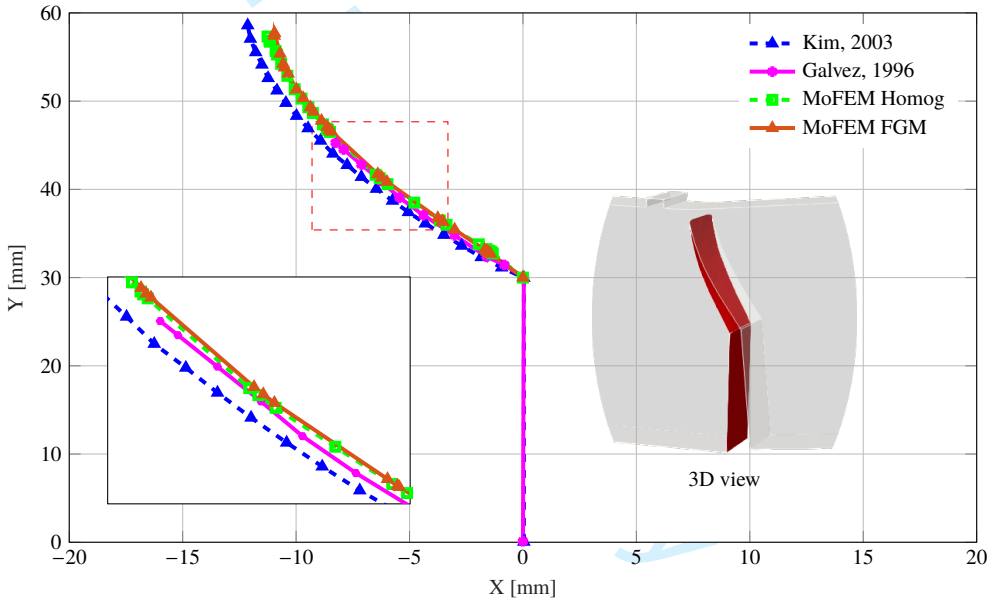

Fig. 10: Comparison of crack paths obtained experimentally by [18], numerically by [40] and by the proposed approach (MoFEM).

rather than a specific traumatic event. Intense exercise and excessive loading of the metacarpal bones results in maladaptation. The location of 3rd metacarpal fractures is remarkably consistent across a large number of racehorses, with crack initiation presenting from the lateral para-sagittal groove of the distal condyle of the leading forelimb [29, 55]. Despite considerable research in the field, including applying diagnostic methods such as radiography [8, 12, 46], magnetic resonance imaging [66] and biomarkers [49], it still remains a challenge to accurately predict the fracture risk and prevent this type of significant injury.

Various theories exist in the literature regarding failure criteria for bone tissue and it is now common practice for researchers to estimate fracture resistance within the framework of FEM. In particular, subject-specific FEM models can potentially quantify the risk of failure under a given loading scenario. However, this still remains an open challenge.

In recent years, the main focus in bone mechanics has been in the use of different strength criteria for the onset of failure. The most commonly adopted ones were based on stress [36] or strain measures [60] assuming bone failure is determined by a yield criterion [69]. Experimental validation of such simplified models show that there is a significant spread in the predicted failure, with errors between 10% and 20% [67]. This variation is perhaps explained by the focus on both the use of strength criteria, rather than energy (as in this paper), and the local initiation of failure, rather than the complete failure mechanism. The fracture process of bone is very important, particularly in the case of fatigue fractures [23]. Limitations in previous studies (e.g. use of 2D geometry [7], assuming homogeneous bone properties [20]), can also explain why an appropriate model for bone fracture has not been developed previously. In contrast to many studies (e.g. [47]), we do not simulate cracks at the microscale, but rather focus on modelling fractures at the macroscale with approximated material properties. Our approach uses the Griffith criterion with maximal energy dissipation principle for evolving crack front, and does not require additional empirical laws which have to be established experimentally.

The material parameters for the following analyses are presented in Table 2. The elastic properties for both cortical and trabecular bone are approximated using a power law derived from mechanical tests of MC3 bone [42]. Such empirical elasticity-density relationships are commonly adopted in finite element investigations of bones [24]. Note that the stress is scaled depending on density as shown in Eq.10, which is equivalent to spatially varying Young's modulus (e.g. like in FGM). Due to lack of experimental data, the fracture energy g_c is assumed constant for the entire domain. Boundary conditions are simplified to two representative forces (5 [kN] each) spanning over a small area based on pressure film studies [9], as illustrated in Figure 11. The two forces are often considered in the literature as an equivalent of joint peak force at the mid-stance of a horse gait. Obviously, with such simplified loading case the analysis is not sufficient to produce any quantitative results regarding critical loading for the metacarpal but rather to demonstrate the potential of this approach. Using a

Param.	Description	Value
E	Young's modulus	4700 [MPa] [42]
ν	Poisson's ratio	0.3 [−]
g_c	Fracture energy	2.0 [N/mm]
n	Porosity exponent	2.25 [−] [42]

Table 2: Material parameters used for the simulations of 3rd metacarpal bone adaptation.

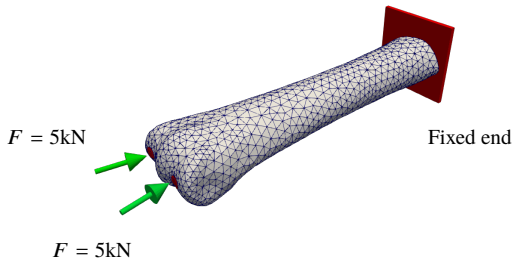

Fig. 11: Finite element mesh of the equine 3rd metacarpal bone. To simulate the peak load of a gallop, 5 kN forces are applied on the lateral and medial side of the distal condyle.

For Review Only

K_2HPO_4 calibration phantom, grey scale values from CT scans are converted to bone mineral density using five tubes with reference densities. The mechanical material properties were mapped onto the integration points of the mesh of the metacarpal bone using the MWLS method described in 3.2. An initial crack was generated in the mesh using a cutting plane, as shown in Figure 12. A notch is situated at the origin of the most common location of a lateral condyle fracture [29]. The adaptive h - p - refinement method described in Section 4.2 proved successful in resolving the propagating crack topology through the challenging bone geometry.

The numerical analyses were undertaken using three meshes consisted of 6069, 10032 and 21189 tetrahedrons and repeated for 1st, 2nd and 3rd-order of global p - refinement and local p - refinement at the crack tip. The finite element meshes were generated by discretising the segmented geometry of a full-scale model of an equine 3rd metacarpal bone derived from CT scan data - see Figure 11. The application of load induces configurational forces at the crack front, as shown in Figure 13. The direction of the vectors also indicates the direction of crack propagation. The values of numerically predicted maximal nodal fracture energy release rates in Mode-I (crack opening) for subsequent meshes are plotted in Figure 14. It can be seen that, for the same mesh, as the order of approximation increases, the energy release rate converges.

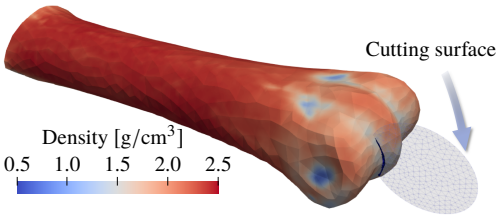

Fig. 12: Bone geometry with density mapped from CT using MWLS. Initial crack introduced by cutting the mesh with a circular surface.

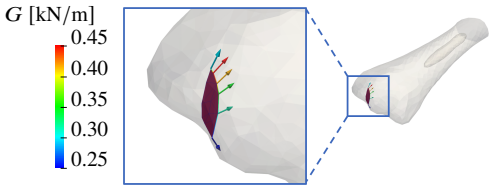

Fig. 13: Crack surface and configurational forces at the crack front.

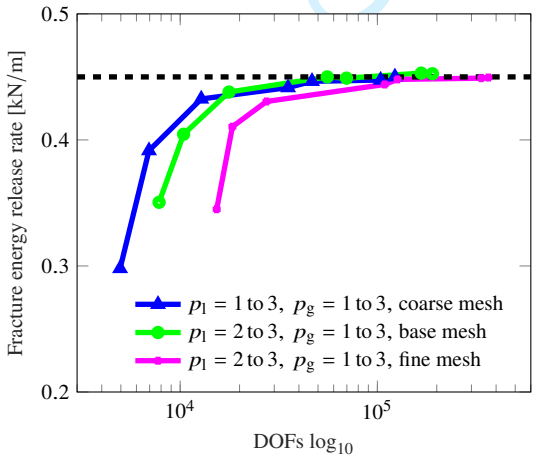

Fig. 14: Convergence plot of fracture energy release rate versus no of DOF (log10) for subsequent discretisations and p - refinements.

A crack will propagate when the energy release rate rate equals the material's resistance to crack extension, g_c. Assuming $g_c = 2.0\,[\mathrm{kN/m}]$ [20], it can be estimated that for this particular metacarpal bone with this initial crack, loading can be increased by a factor of approximately 4.4 before a fracture starts to propagate.

5.4 Crack propagation in bone

In this section, we take the analysis further by simulating the full process of crack propagation in equine bone. The magnitude of applied forces (Figure 11) is controlled by the increment in crack area during each load step using an arc-length technique. The initial finite element mesh is the same as previously, although it is locally refined as the crack front advances. The heterogeneous density distribution is mapped from CT scan data. The mesh comprises 2nd order tetrahedral elements. The numerically predicted crack path is shown in Figure 15. It can be seen that the crack shape is initially planar before curving towards the lateral side of the bone. This simulated crack path compares well with fractures observed in radiographs [68], especially considering the simplified loading conditions. The load factor versus crack area plot is shown in Figure 16(a). Figure 16(a)

Fig. 15: Crack surface evolution in equine 3rd metacarpal.

compares results with and without using singularity element. Although the singularity element improves the accuracy of stresses at the crack front, as previously demonstrated (Figure 5(b)), it is evident that it has negligible influence on the overall response. Figure 16(b) compares the results with heterogeneous material properties to results with homogeneous properties. From the load-crack area curves, it can be observed that the heterogeneous nature of bone has a significant impact on the predicted response and crack path.

Finally, we investigated h and p convergence. The results presented on the Figures 17(a) and 17(b) show good numerical convergence for consecutive refinements. It can be concluded that our formulation predicts the crack path accurately with minimal effect from the original mesh or order of approximation. It is important to note that bone is generally regarded as a quasi-brittle material [20]. Therefore, the assumption of linear fracture mechanics has limited applicability and further developments should include cohesive effects, such as collagen fibre bridging.

6 Discussion

This paper has presented a mathematical formulation and computational modelling framework to investigate the influence of heterogeneous material properties on fracture resistance and fracture propagation. This was

For Review Only

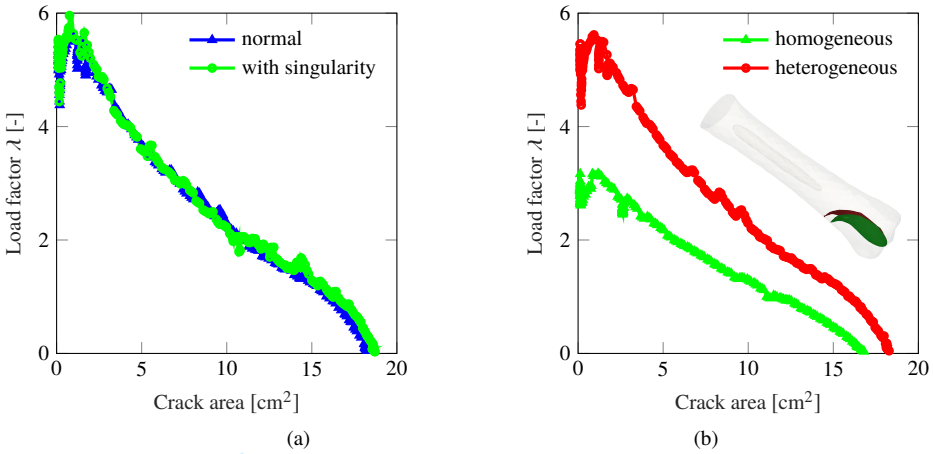

Fig. 16: Load factor versus crack area for (a) with and without singularity element and (b) homogeneous versus heterogeneous density distribution.

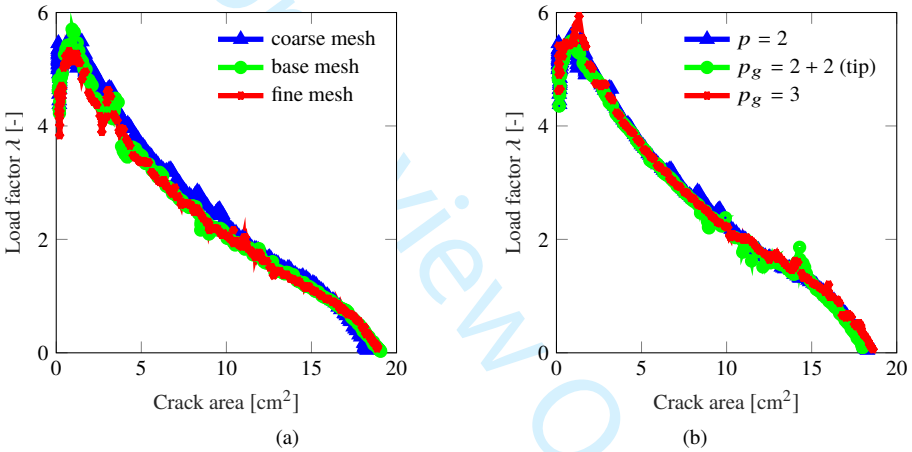

Fig. 17: Load factor versus crack area (a) h - refinement). (b) p - refinement.

achieved through an extension of the authors' previous work on configurational mechanics for fracture, based on the assumption of maximal dissipation of energy and utilising the Griffith criterion. With no additional physical equations or material laws, this has been shown to be sufficient for modelling this class of problem. Configurational forces are the driver for crack propagation and it was shown that in order to evaluate correctly these forces at the crack front it is necessary to have a spatially smooth density field, with higher regularity than if the field is directly approximated on the finite element mesh. Therefore, density data is approximated as a smooth field using a Moving Weighted Least Squares method. In this paper, the density fields were generated analytically, for FGMs, and from clinically available CT scan data for equine bone. It is important to note that the adoption of configurational mechanics avoids the need for post-processing, since configurational forces are expressed exclusively in terms of nodal quantities.

Numerical examples demonstrated the performance and accuracy of the proposed framework. Numerical convergence was demonstrated and the use of singularity elements was shown to further improve the rate of convergence. However, it was also confirmed that improved accuracy of the stress at the crack front had no impact on the crack propagation analysis and the resulting crack path. Analyses of functionally graded materials showed

For Review Only

the ability of the proposed method to simulate experimental crack paths. The final example, demonstrated how mechanical loading influence the resistances to bone fracture while using experimental material data. Therefore, this framework will be a useful tool in understanding fractures in bone and ultimately preventing catastrophic fractures.

All analyses were undertaken using the MoFEM library [33] that has been developed to support computational scalability and ensure robustness. The entire framework can be executed on parallel computer systems. Supplementary data (CT scans, mesh files, command lines) necessary to reproduce the results of all numerical examples can be found in [43]. The fracture submodule in MoFEM [33], can be installed using the flexible package manager, Spack [19].

References

1. M. Ainsworth and J. Coyle. Hierarchic finite element bases on unstructured tetrahedral meshes. *International Journal for Numerical Methods in Engineering*, 58(14):2103–2130, 2003.
2. A. Ayhan. Three-dimensional mixed-mode stress intensity factors for cracks in functionally graded materials using enriched finite elements. *International Journal of Solids and Structures*, 46(3-4):796–810, 2009.
3. I. Babuska, U. Banerjee, and K. Kergrene. Strongly stable generalized finite element method: Application to interface problems. *Computer Methods in Applied Mechanics and Engineering*, 327(SI):58–92, 2017.
4. R. S. Barsoum. On the use of isoparametric finite elements in linear fracture mechanics. *International Journal for Numerical Methods in Engineering*, 10(1):25–37, 1976.
5. H. Bayesteh and S. Mohammadi. XFEM fracture analysis of orthotropic functionally graded materials. *Composites Part B-Engineering*, 44(1):8–25, 2013.
6. T. Belytschko and T. Black. Elastic crack growth in finite elements with minimal remeshing. *International Journal for Numerical Methods in Engineering*, 45(5):601–620, 1999.
7. A. Bettamer, R. Hambli, S. Allaoui, and A. Almhdie-Imjabber. Using visual image measurements to validate a novel finite element model of crack propagation and fracture patterns of proximal femur. *Computer Methods in Biomechanics and Biomedical Engineering: Imaging & Visualization*, 5(4):251–262, 2017.
8. S. H. Bogers, C. W. Rogers, C. Bolwell, W. Roe, E. Gee, and C. W. McIlwraith. Quantitative comparison of bone mineral density characteristics of the distal epiphysis of third metacarpal bones from thoroughbred racehorses with or without condylar fracture. *American Journal of Veterinary Research*, 77(1):32–38, 2016.
9. P. Brama, D. Karssenberg, A. Barneveld, and P. Van Weeren. Contact areas and pressure distribution on the proximal articular surface of the proximal phalanx under sagittal plane loading. *Equine Veterinary Journal*, 33(1):26–32, 2001.
10. M. Chafi and A. Boulenouar. A Numerical Modelling of Mixed Mode Crack Initiation and Growth in Functionally Graded Materials. *Materials Research-Ibero-American Journal of Materials*, 22(3), 2019.
11. W. Chang-chun, H. Peixiang, and L. Ziran. Extension of J integral to dynamic fracture of functional graded material and numerical analysis. *Computers & Structures*, 80(5):411–416, 2002.
12. C. Crijns, A. Martens, H.-J. Bergman, H. van der Veen, L. Duchateau, H. van Bree, and I. Gielen. Intramodality and intermodality agreement in radiography and computed tomography of equine distal limb fractures. *Equine Veterinary Journal*, 46(1):92–96, 2014.
13. J. W. Eischen. Fracture of nonhomogeneous materials. *International Journal of Fracture*, 34(1):3–22, 1987.
14. F. Erdogan. Fracture-Mechanics of Functionally Graded Materials. *Composites Engineering*, 5(7):753–770, 1995.
15. J. D. Eshelby. The force on an elastic singularity. *Phil. Trans. R. Soc. Lond. A*, 244(877):87–112, 1951.
16. M. Finot and S. Suresh. Small and large deformation of thick and thin-film multi-layers: Effect of layer geometry, plasticity and compositional gradients. *Journal of the Mechanics and Physics of Solids*, 44(5):683–721, 1996.

For Review Only

17. F. D. Fischer, J. Predan, R. Müller, and O. Kolednik. On problems with the determination of the fracture resistance for materials with spatial variations of the Young's modulus. *International Journal of Fracture*, 190(1):23–38, 2014.
18. J. Galvez, M. Elices, G. Guinea, and J. Planas. Crack trajectories under mixed mode and non-proportional loading. *International Journal of Fracture*, 81(2):171–193, 1996.
19. T. Gamblin, M. LeGendre, M. R. Collette, G. L. Lee, A. Moody, B. R. de Supinski, and S. Futral. The Spack Package Manager: Bringing Order to HPC Software Chaos. In *Proceedings of the International Conference for High Performance Computing, Networking, Storage and Analysis*, SC '15, pages 40:1–40:12, New York, NY, USA, 2015. ACM.
20. T. C. Gasser and G. A. Holzapfel. A numerical framework to model 3-d fracture in bone tissue with application to failure of the proximal femur. In *IUTAM Symposium on Discretization Methods for Evolving Discontinuities*, pages 199–211. Springer, 2007.
21. L. J. Gibson. Biomechanics of cellular solids. *Journal of Biomechanics*, 38(3):377–399, 2005.
22. A. A. Griffith. The Phenomena of Rupture and Flow in Solids. *Philosophical Transactions of the Royal Society of London A: Mathematical, Physical and Engineering Sciences*, 221(582-593):163–198, 1921.
23. H. Gupta and P. Zioupos. Fracture of bone tissue: the 'hows' and the 'whys'. *Medical Engineering & Physics*, 30(10):1209–1226, 2008.
24. B. Helgason, E. Perilli, E. Schileo, F. Taddei, S. Brynjolfsson, and M. Viceconti. Mathematical relationships between bone density and mechanical properties: a literature review. *Clinical Biomechanics*, 23(2):135–146, 2008.
25. B. Helgason, F. Taddei, H. Pálsson, E. Schileo, L. Cristofolini, M. Viceconti, and S. Brynjólfsson. A modified method for assigning material properties to FE models of bones. *Medical Engineering and Physics*, 30(4):444–453, 2008.
26. R. Henshell and K. Shaw. Crack tip finite elements are unnecessary. *International Journal for Numerical Methods in Engineering*, 9(3):495–507, 1975.
27. Hirshikesh, S. Natarajan, R. Annabattula, and E. Martinez-Paneda. Phase field modelling of crack propagation in functionally graded materials. *Composites Part B-Engineering*, 169:239–248, 2019.
28. J. M. Hughes, K. L. Popp, R. Yanovich, M. L. Bouxsein, and R. W. Matheny Jr. The role of adaptive bone formation in the etiology of stress fracture. *Experimental Biology and Medicine*, 242(9):897–906, 2017.
29. B. Jacklin and I. Wright. Frequency distributions of 174 fractures of the distal condyles of the third metacarpal and metatarsal bones in 167 Thoroughbred racehorses (1999–2009). *Equine Veterinary Journal*, 44(6):707–713, 2012.
30. D. Jha, T. Kant, and R. Singh. A critical review of recent research on functionally graded plates. *Composite Structures*, 96:833–849, 2013.
31. Ł. Kaczmarczyk, M. M. Nezhad, and C. Pearce. Three-dimensional brittle fracture: configurational-force-driven crack propagation. *International Journal for Numerical Methods in Engineering*, 97(7):531–550, 2014.
32. L. Kaczmarczyk and C. Pearce. Efficient numerical analysis of bone remodelling. *Journal of the Mechanical Behavior of Biomedical Materials*, 4(6):858 – 867, 2011. Bone Remodeling.
33. Ł. Kaczmarczyk, Z. Ullah, K. Lewandowski, X. Meng, X.-Y. Zhou, I. Athanasiadis, H. Nguyen, C.-A. Chalons-Mouriesse, E. Richardson, E. Miur, A. Shvarts, M. Wakeni, and C. Pearce. MoFEM: an open source, parallel finite element library. *The Journal of Open Source Software*, 2020. http://mofem.eng.gla.ac.uk.
34. Ł. Kaczmarczyk, Z. Ullah, and C. J. Pearce. Energy consistent framework for continuously evolving 3d crack propagation. *Computer Methods in Applied Mechanics and Engineering*, 324:54–73, 2017.
35. A. Kawasaki and R. Watanabe. Concept and P/M fabrication of functionally gradient materials. *Ceramics International*, 23(1):73–83, 1997.
36. J. H. Keyak, T. S. Kaneko, J. Tehranzadeh, and H. B. Skinner. Predicting proximal femoral strength using structural engineering models. *Clinical Orthopaedics and Related Research®*, 437:219–228, 2005.
37. R. Kienzler and G. A. Maugin. *Configurational mechanics of materials*, volume 427. Springer, 2014.

For Review Only

38. J. Kim and G. Paulino. Finite element evaluation of mixed mode stress intensity factors in functionally graded materials. *International Journal for Numerical Methods in Engineering*, 53(8):1903–1935, 2002.
39. J. Kim and G. Paulino. Simulation of crack propagation in functionally graded materials under mixed-mode and non-proportional loading. *Composite Structures*, 1:63–94, 2004.
40. J.-H. Kim and G. H. Paulino. Simulation of crack propagation in functionally graded materials under mixed-mode and non-proportional loading. *Mechanics and Materials in Design*, 1(1):63–94, 2004.
41. E. Kuhl and P. Steinmann. Theory and numerics of geometrically non-linear open system mechanics. *International Journal for Numerical Methods in Engineering*, 58(11):1593–1615, 2003.
42. C. M. Les, J. H. Keyak, S. M. Stover, K. T. Taylor, and A. J. Kaneps. Estimation of material properties in the equine metacarpus with use of quantitative computed tomography. *Journal of Orthopaedic Research*, 12(6):822–833, 1994.
43. K. Lewandowski. Supplement data for Numerical investigation into fracture risk of bone following adaptation, Dec. 2019.
44. K. Lewandowski, Łukasz Kaczmarczyk, I. Athanasiadis, and C. Pearce. Moving Weighted Least Squares implementation in MoFEM. 2019.
45. S. Loehnert, D. S. Mueller-Hoeppe, and P. Wriggers. 3D corrected XFEM approach and extension to finite deformation theory. *International Journal for Numerical Methods in Engineering*, 86, 2011.
46. A. Loughridge, A. Hess, T. Parkin, and C. Kawcak. Qualitative assessment of bone density at the distal articulating surface of the third metacarpal in thoroughbred racehorses with and without condylar fracture. *Equine Veterinary Journal*, 49(2):172–177, 2017.
47. M. Marco, R. Belda, M. H. Miguélez, and E. Giner. A heterogeneous orientation criterion for crack modelling in cortical bone using a phantom-node approach. *Finite Elements in Analysis and Design*, 146:107–117, 2018.
48. G. A. Maugin. *Configurational forces: thermomechanics, physics, mathematics, and numerics*. Chapman and Hall/CRC, 2016.
49. C. McIlwraith. Use of synovial fluid and serum biomarkers in equine bone and joint disease: a review. *Equine Veterinary Journal*, 37(5):473–482, 2005.
50. M. Naebe and K. Shirvanimoghaddam. Functionally graded materials: A review of fabrication and properties. *Applied Materials Today*, 5:223–245, 2016.
51. M. Nejati, A. Paluszny, and R. W. Zimmerman. On the use of quarter-point tetrahedral finite elements in linear elastic fracture mechanics. *Engineering Fracture Mechanics*, 144:194–221, 2015.
52. E. Ooi, S. Natarajan, C. Song, and F. Tin-Loi. Crack propagation modelling in functionally graded materials using scaled boundary polygons. *International Journal of Fracture*, 192(1):87–105, 2015.
53. K. Özenç, G. Chinaryan, and M. Kaliske. A configurational force approach to model the branching phenomenon in dynamic brittle fracture. *Engineering Fracture Mechanics*, 157:26–42, 2016.
54. T. Parkin, P. Clegg, N. French, C. Proudman, C. Riggs, E. Singer, P. Webbon, and K. Morgan. Risk of fatal distal limb fractures among thoroughbreds involved in the five types of racing in the United Kingdom. *The Veterinary Record*, 154(16):493–497, 2004.
55. T. Parkin, P. Clegg, N. French, C. Proudman, C. Riggs, E. Singer, P. Webbon, and K. Morgan. Analysis of horse race videos to identify intra-race risk factors for fatal distal limb fracture. *Preventive Veterinary Medicine*, 74(1):44–55, 2006.
56. T. D. H. Parkin, P. D. Clegg, N. P. French, C. J. Proudman, C. M. Riggs, E. R. Singer, P. M. Webbon, and K. L. Morgan. Risk factors for fatal lateral condylar fracture of the third metacarpus/metatarsus in UK racing. *Equine Veterinary Journal*, 37(3):192–199, 2005.
57. S. Poelert, E. Valstar, H. Weinans, and A. A. Zadpoor. Patient-specific finite element modeling of bones. *Proceedings of the Institution of Mechanical Engineers, Part H: Journal of Engineering in Medicine*, 227(4):464–478, 2013.
58. D. P. Rooke and D. J. Cartwright. Compendium of stress intensity factors. *Procurement Executive, Ministry of Defence. H. M. S. O. 1976, 330 p(Book).*, 1976.
59. C.-E. Rousseau and H. Tippur. Compositionally graded materials with cracks normal to the elastic gradient. *Acta Materialia*, 48(16):4021–4033, 2000.

For Review Only

60. E. Schileo, F. Taddei, L. Cristofolini, and M. Viceconti. Subject-specific finite element models implementing a maximum principal strain criterion are able to estimate failure risk and fracture location on human femurs tested in vitro. *Journal of Biomechanics*, 41(2):356–367, 2008.
61. M. Shi, H. Wu, L. Li, and G. Chai. Calculation of stress intensity factors for functionally graded materials by using the weight functions derived by the virtual crack extension technique. *International Journal of Mechanics and Materials in Design*, 10(1):65–77, 2014.
62. S. Shojaee and A. Daneshmand. Crack analysis in media with orthotropic Functionally Graded Materials using extended Isogeometric analysis. *Engineering Fracture Mechanics*, 147:203–227, 2015.
63. P. Steinmann, D. Ackermann, and F. Barth. Application of material forces to hyperelastostatic fracture mechanics. II. Computational setting. *International Journal of Solids and Structures*, 38(32-33):5509–5526, 2001.
64. F. Taddei, E. Schileo, B. Helgason, L. Cristofolini, and M. Viceconti. The material mapping strategy influences the accuracy of CT-based finite element models of bones: an evaluation against experimental measurements. *Medical Engineering & Physics*, 29(9):973–979, 2007.
65. R. Tian, L. Wen, and L. Wang. Three-dimensional improved XFEM (IXFEM) for static crack problems. *Computer Methods in Applied Mechanics and Engineering*, 343:339–367, 2019.
66. C. Tranquille, R. Murray, and T. Parkin. Can we use subchondral bone thickness on high-field magnetic resonance images to identify Thoroughbred racehorses at risk of catastrophic lateral condylar fracture? *Equine Veterinary Journal*, 49(2):167–171, 2017.
67. S. van den Munckhof and A. A. Zadpoor. How accurately can we predict the fracture load of the proximal femur using finite element models? *Clinical Biomechanics*, 29(4):373–380, 2014.
68. R. C. Whitton, G. D. Trope, A. Ghasem-Zadeh, G. A. Anderson, T. D. Parkin, E. J. Mackie, and E. Seeman. Third metacarpal condylar fatigue fractures in equine athletes occur within previously modelled subchondral bone. *Bone*, 47(4):826–831, 2010.
69. Z. Yosibash, D. Tal, and N. Trabelsi. Predicting the yield of the proximal femur using high-order finite-element analysis with inhomogeneous orthotropic material properties. *Philosophical Transactions of the Royal Society of London A: Mathematical, Physical and Engineering Sciences*, 368(1920):2707–2723, 2010.
70. C. Zannoni, R. Mantovani, and M. Viceconti. Material properties assignment to finite element models of bone structures: a new method. *Medical Engineering & Physics*, 20(10):735–740, 1999.
71. C. Zhang, M. Cui, J. Wang, X. Gao, J. Sladek, and V. Sladek. 3D crack analysis in functionally graded materials. *Engineering Fracture Mechanics*, 78(3, SI):585–604, 2011.

For Review Only